

# Nonlinear dynamics of earthquake-resistant structures using shape memory alloy composites

Lucas L Vignoli<sup>1,2</sup>, Marcelo A Savi<sup>1</sup>  and Sami El-Borgi<sup>3</sup>

Journal of Intelligent Material Systems and Structures

2020, Vol. 31(5) 771–787

© The Author(s) 2020

Article reuse guidelines:

sagepub.com/journals-permissions

DOI: 10.1177/1045389X19898269

journals.sagepub.com/home/jim



## Abstract

Earthquake-resistant structures have been widely investigated in order to produce safe buildings designed to resist seismic activities. The remarkable properties of shape memory alloys, especially pseudoelastic effect, can be exploited in order to promote the essential energy dissipation necessary for earthquake-resistant structures. In this regard, shape memory alloy composite is an idea that can make this application feasible, using shape memory alloy fibers embedded in a matrix. This article investigates the use of shape memory alloy composites in a one-story frame structure subjected to earthquakes. Different kinds of composites are analyzed, comparing the influence of matrix type. Both linear elastic matrix and elastoplastic matrix with isotropic and kinematic hardening are investigated. Results indicate the great energy dissipation capability of shape memory alloy composites. A parametric analysis allows one to conclude that the maximum shape memory alloy volume fraction is not the optimum design condition for none of the cases studied, highlighting the necessity of a proper composite design. Despite the elastoplastic behavior of matrix also dissipates a considerable amount of energy, the associated residual strains are not desirable, showing the advantage of the use of shape memory alloys.

## Keywords

Shape memory alloy, composite, smart structures, nonlinear dynamics, earthquake, seismic loads

## 1. Introduction

Seismic activity is a natural phenomenon that can be related to catastrophic consequences. Since 2000, it was registered between 1300 and 2500 earthquakes with a magnitude greater than 5 on the Richter scale worldwide every year (see Figure 1). This scenario causes an average of 50,102 deaths per year (U.S. Geological Survey, 2019). Some reports describing damages due to earthquakes can be found in Padgett et al. (2008) and DesRoches et al. (2011). In this regard, earthquake-resistant structures have an especial importance in order to reduce the severe effects of seismic activities. The main idea is to build structures that can resist to seismic activities better than the usual ones, avoiding critical damages. Several approaches are employed for this aim.

Bridges usually adopt hinge restrainers to perform joint frames. DesRoches and Fenves (2000) proposed a methodology for the design of these restrainers, decreasing the earthquake effects. The application of viscoelastic dampers on the structural basis is investigated by Xu (2007) and later extended by Xu (2009)

and Xu et al. (2017) where multidirectional load conditions are considered.

Structural retrofit is an interesting approach employed on earthquake-resistant structures. Yeghneim et al. (2009) suggested the application of composite plates bonded in shear wall structures in order to improve the structural stiffness and strength. Kim and Jeong (2016) suggested the coupling of steel plates able to slip, inducing damping. Colalillo and Sheikh (2012)

<sup>1</sup>Center for Nonlinear Mechanics, COPPE – Department of Mechanical Engineering, Universidade Federal do Rio de Janeiro, Rio de Janeiro, Brazil

<sup>2</sup>Center for Technology and Application of Composite Materials, Department of Mechanical Engineering, Universidade Federal do Rio de Janeiro, Rio de Janeiro, Brazil

<sup>3</sup>Mechanical Engineering Program, Texas A&M University at Qatar, Doha, Qatar

### Corresponding author:

Marcelo A Savi, Center for Nonlinear Mechanics, COPPE – Department of Mechanical Engineering, Universidade Federal do Rio de Janeiro, P.O. Box 68.503, Rio de Janeiro 21.941.972, Brazil.  
Email: savi@mecanica.coppe.ufrj.br

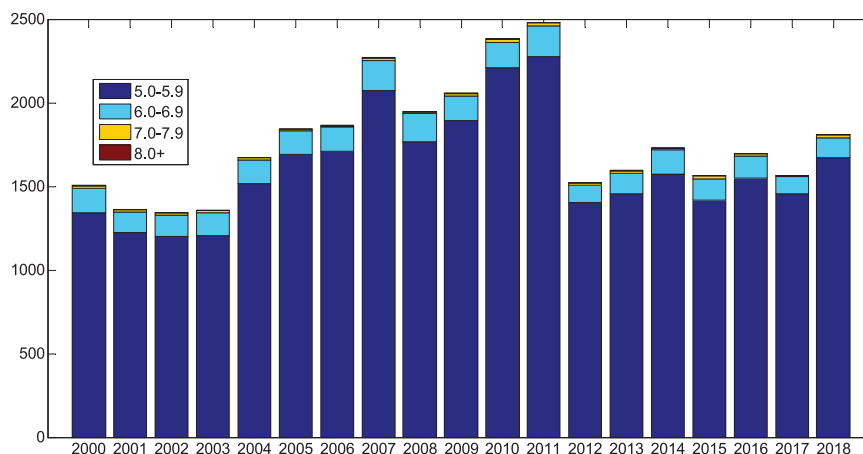


**Figure 1.** Amount of earthquake per year (U.S. Geological Survey, 2019).

promoted shear strength increase by considering reinforced bonded fiber. An additional important device developed with this purpose is the friction pendulum system, which isolates seismic ground motion by bearings (Eröz and DesRoches, 2008).

Structures with variable stiffness and damping are an alternative widely investigated to enhance resistance. Sahasrabudhe and Nagarajaiah (2005) proposed a variable stiffness device built with a set of four springs. The system is able to change the directions of these springs by active control, varying its stiffness according to the load condition.

The use of smart materials is another possibility to build earthquake-resistant structures. Basically, smart materials present a coupling among different physical fields, being characterized by adaptive behavior. In brief, piezoelectric materials, magnetorheological fluids, and shape memory alloys (SMAs) are candidates for this kind of application.

The remarkable properties of SMA devices can be employed exploiting either phase transformations or property changes. SMA dynamical systems usually present a rich, complex behavior that can be used for both passive and active control. For instance, Zhang et al. (2017) and Zhang et al. (2019) investigated SMA beam stability and Rodrigues et al. (2017) and Fonseca et al. (2019) investigated nonlinear dynamics of SMA origami structures. A general overview of the nonlinear dynamics of SMA systems is presented by Savi (2015).

Energy dissipation capacity is the essential characteristic to be employed for earthquake-resistant structures (Asgarian et al., 2016; Cardone and Dolce, 2009; Qian et al., 2013; Yang et al., 2010). Pseudoelasticity offers an intrinsic energy dissipation due to its hysteretic behavior and, when compared to the plasticity of traditional materials, it has the advantage to be not related to irreversible residual strains (Baratta and Corbi, 2002).

Khodaverdian et al. (2012) explored the combination of energy dissipation due to friction and SMA

behavior. A steel–polytetrafluoroethylene (PTFE)-bearing device is proposed to be installed on the connection between bridge-span and piers using SMA wires to link both parts of the bar, increasing the energy dissipation capability. The use of SMA to improve frictional dissipation is also possible by considering two blocks in contact and attached to the structure with SMA wires promoting the connection of these blocks (Zhang and Zhu, 2007).

Smart material adaptability is also employed in order to produce stiffness and damping variations. In this regard, magnetorheological (Li et al., 2013; Xu and Guo, 2006) and piezoelectric (Lu and Lin, 2009) are interesting possibilities where the main challenge is the control capability. Rabiee and Chae (2019) presented a discussion about this issue, proposing a novel approach to control the variable friction devices.

The use of shape memory alloy composite (SMAC) considering SMA fibers embedded in a matrix is an attractive idea that allows the combination of different materials for an interesting structure performance. For a detailed discussion about perspectives and applications of SMAC, see Lester et al. (2015). Billah and Alam (2012) investigated the combination of SMA and carbon fiber polymeric bars embedded in a concrete column to promote vibration absorption. Zafar and Andrawes (2015) joined SMA and glass fibers in a polymeric matrix to build bars used to reinforce concrete structure in horizontal and vertical directions. Alternatively, Abou-Elfath (2017) highlighted that a hybrid brace built by SMA and steel may improve the capability to seismic load resistance. An arrangement of SMA and steel wires is modeled, but the conclusions can also be extended for composites with SMA inclusions in metallic matrix. The analysis of martensite–austenite phase transformation is not explicitly indicated in these investigations pointing to the necessity of this analysis for a more general

comprehension of the use of SMA composites on earthquake-resistant structures.

The design of composite materials requires a deep analysis due to the great number of variables involved (Tsai and Melo, 2014; Vignoli et al., 2019). Although there are some experimental reports indicating the improvement on the earthquake resistance capability with pure SMA (Boroschek et al., 2007; Dolce et al., 2005; Johnson et al., 2008; Shrestha et al., 2015) and composite with SMA fibers (Nehdi et al., 2010), a detailed parametric study becomes a fundamental tool to understand the structural response for the design of SMAC.

Earthquake-resistant structures are usually analyzed from archetypal models as the  $n$ -story frames (Ozbulut et al., 2011; Saadat et al., 2001; Ozbulut and Hurlebaus, 2012). The use of diagonal braces that can reinforce the structure is especially attractive due to the ease of coupling. Yan et al. (2013) presented numerical and experimental studies of three-story frames with SMA braces, comparing four different conditions: without reinforced braces, with braces just on the first floor, with braces on the two first floors, and with braces in all the floors. Despite the addition of braces in more than one floor decreases the amplitude of oscillation, the martensitic volume fraction variation is difficult to be measured and therefore, it is not possible to conclude whether this effect is due to pseudoelasticity or the increased stiffness.

This article deals with the dynamical analysis of an earthquake-resistant structure built with SMAC elements. A model of a one-story structure subjected to seismic loads is of concern, considering SMAC braces. Nonlinear dynamics of a reduced order model, a single-degree-of-freedom oscillator, is analyzed considering the restitution force provided by the SMAC. Micromechanics analysis allows one to propose a macroscopic model for the composite response. A parametric analysis is carried out treating the influence of SMA volume fraction on the structural response. In addition, the influence of the matrix type is discussed considering two matrix models: a linear elastic polymer and an elastoplastic aluminum. The possibility to join SMA and other fibers (e.g. glass and carbon) is also investigated, evaluating different stiffness and plastic effects. A detailed discussion about the stress–strain, martensite evolution, displacement, and energy dissipated according to the time is reported allowing a proper comprehension of the system behavior. The structure is subjected to an earthquake loading process based on the ground acceleration data of the El Centro earthquake (18 May 1940—Imperial Valley, USA) with magnitude 7.1 on the Richter scale. Numerical simulations show the great energy dissipation capability of SMA composites establishing the optimum design condition and the advantage of the use of composite materials.

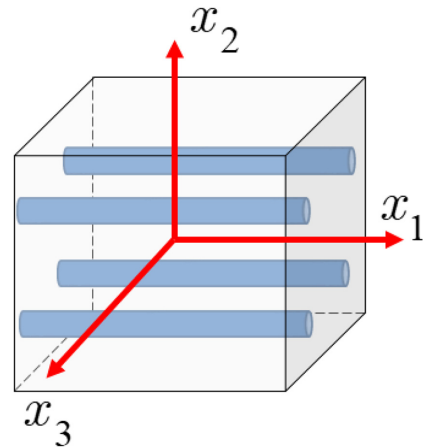


**Figure 2.** Unidirectional composite with SMA fibers.

## 2. SMA composite model

The mathematical model for a SMAC considers a constitutive model that describes the thermomechanical behavior of SMAs together with a homogenization approach to describe the composite material. Three basic assumptions are assumed for this aim: uniform and constant temperature on the composite; both constituents have the same strain; and the load is shared between matrix and fibers to provide equilibrium requirement. Both kinematics and equilibrium considerations are regarded as the longitudinal direction  $x_1$  (Figure 2). Under these assumptions, it is written that

$$\varepsilon_{sma} = \varepsilon_m = \varepsilon \quad (1)$$

$$V_{sma}\sigma_{sma} + (1 - V_{sma})\sigma_m = \sigma \quad (2)$$

where the index  $m$  denotes matrix while  $sma$  denotes SMA,  $\varepsilon$  is the strain, and  $\sigma$  is the stress. The absence of index is used to denote the equivalent macroscopic quantity of the composite material.  $V_{sma}$  is the SMA volume fraction and  $V_m = 1 - V_{sma}$  is the matrix volume fraction. It should be pointed out that it is assumed no voids on the microstructure.

### 2.1. SMA model

In order to proceed with the derivation of the composite modeling, an SMA constitutive model needs to be employed. There are several possibilities for this aim. Lagoudas (2008) and Paiva and Savi (2006) performed a general overview of some phenomenological possibilities. Considering more recent alternatives, it is interesting to cite Oliveira et al. (2016, 2018) and Cisse et al. (2016). Ghodke and Jangid (2016) proposed a simplified method to compute equivalent linear stiffness and damping of SMAs.

Based on the discussion presented by Paiva and Savi (2006), Brinson's model (Brinson, 1993) is chosen in this article, introducing some modifications proposed by Enemark et al. (2014). Since pseudoelastic effect is in focus, just mechanical loads are of concern and temperature is assumed to be constant. Under this assumption, stress–strain ( $\sigma$ – $\varepsilon$ ) relation is given by

$$\sigma_{sma} - \sigma_{sma}^0 = (E_{sma}\varepsilon_{sma} - E_{sma}^0\varepsilon_{sma}^0) - \varepsilon_R(E_{sma}\beta - E_{sma}^0\beta) \quad (3)$$

where  $\beta$  represents martensitic volume fraction. The original model due to Brinson (1993) considers that this variable is split into twinned martensite induced by temperature ( $\beta_T$ ) and detwinned martensite induced by stress ( $\beta_S$ ). This variable is defined in such a way that  $0 \leq \beta \leq 1$ . Since pseudoelastic effect is in focus,  $\beta_T = 0$ , and in order to treat either tension or compression behaviors, it is assumed that  $-1 \leq \beta \leq 1$ . This means that positive values are related to tension-induced detwinned martensite while negative values are related to compression-induced detwinned martensite. Besides,  $E_{sma} = E_{sma}(\beta) = E_A + |\beta|(E_M - E_A)$  is the SMA equivalent elastic modulus, with  $E_A$  and  $E_M$  representing the austenite and martensite elastic moduli, respectively;  $\varepsilon_R$  is the maximum recoverable strain due to thermal treatment. The upper index "0" denotes the initial state. Phase transformation kinetics is represented by cosine functions for austenite–martensite and reverse transformations (Brinson, 1993).

The forward transformation ( $A \rightarrow M^\pm$ ) is defined in the interval  $\sigma_{fs} \leq |\sigma_{sma}| \leq \sigma_{ff}$ , where the stress limits are  $\sigma_{fs} = C_M(T - M_s)$  and  $\sigma_{ff} = C_M(T - M_f)$ . Therefore, the martensitic volume fraction is defined by

$$\beta = \beta_0 + [\text{sign}(\sigma_{sma}) - \beta_0] f_M(\tilde{\sigma}) \quad (4)$$

where the hardening function is defined by a Bézier curve

$$f_M(\tilde{\sigma}) = f(\tilde{\sigma}, n_1^f, n_2^f) \quad (5)$$

where  $\tilde{\sigma} = (|\sigma_{sma}| - \sigma_{fs}) / (\sigma_{ff} - \sigma_{fs})$  and parameters  $n_1^f$  and  $n_2^f$  are adjusted to fit experimental data. The use of Bézier curves are based on the proposition of Enemark et al. (2014) and Enemark et al. (2016), being presented in its general form as follows (note the use of general parameters  $n_1$  and  $n_2$ )

$$f(\tilde{\sigma}, n_1, n_2) = \begin{cases} \frac{1}{2}s_1^2 & \text{if } 0 \leq \tilde{\sigma} \leq b \\ 1 - \frac{1}{2}s_2^2 & \text{if } b < \tilde{\sigma} \leq 1 \end{cases} \quad (6)$$

where  $b$ ,  $s_1$ , and  $s_2$  are given by

$$b = \frac{1}{2}(n_1 - n_2 + 1) \quad (7)$$

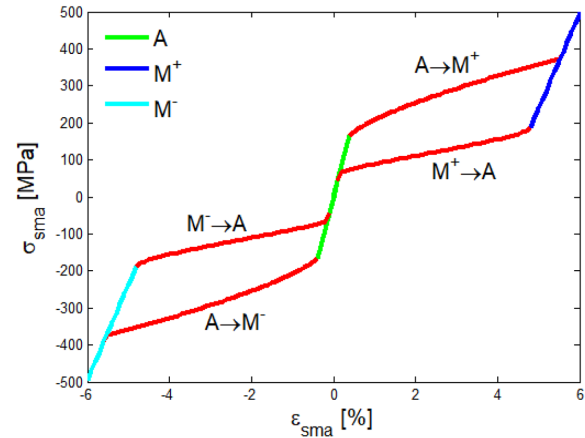


**Figure 3.** Stress–strain curve of the SMA representing the pseudoelastic behavior.

**Table 1.** SMA properties (Alves et al., 2018; Enemark et al., 2014).

$\varepsilon_R$ (%)	$E_A$ (GPa)	$E_M$ (GPa)	$C_A$ (MPa/°C)	$C_M$ (MPa/°C)
4.08	44.5	25.8	7.70	11.84
$A_s$ (°C)	$A_f$ (°C)		$M_s$ (°C)	$M_f$ (°C)
0.8	17		11.8	−6.5
$n_1^f$	$n_2^f$		$n_1^r$	$n_2^r$
0.286	0.001		0.166	0.280

SMA: shape memory alloy.

$$s_1 = \frac{-n_1 + \sqrt{n_1^2 + (b - 2n_1)\tilde{\sigma}}}{b - 2n_1} \quad (8)$$

$$s_2 = \frac{n_2 - \sqrt{n_2^2 - (b + 2n_2 - 1)(1 - \tilde{\sigma})}}{b + 2n_2 - 1} \quad (9)$$

For the reverse transformation ( $M^\pm \rightarrow A$ ), the interval is  $\sigma_{rf} \leq |\sigma_{sma}| \leq \sigma_{rs}$ , where  $\sigma_{rf} = C_A(T - A_f)$  and  $\sigma_{rs} = C_A(T - A_s)$ . Therefore, the volume fraction is defined by

$$\beta = \beta_0 f_A(\tilde{\sigma}) \quad (10)$$

$$f_A(\tilde{\sigma}) = f(\tilde{\sigma}, n_1^r, n_2^r) \quad (11)$$

where the hardening function is again based on the Bézier curves defined in equation (6), but using  $\tilde{\sigma} = (|\sigma_{sma}| - \sigma_{rf}) / (\sigma_{rs} - \sigma_{rf})$  together with the adjustable parameters  $n_1^r$  and  $n_2^r$ .

SMA stress–strain curve presents a pseudoelastic behavior characterized by a hysteresis loop. Figure 3 shows the stress–strain curve of an SMA specimen subjected to tension/compression loads with properties listed in Table 1, where  $A_s$  and  $A_f$  are the starting and

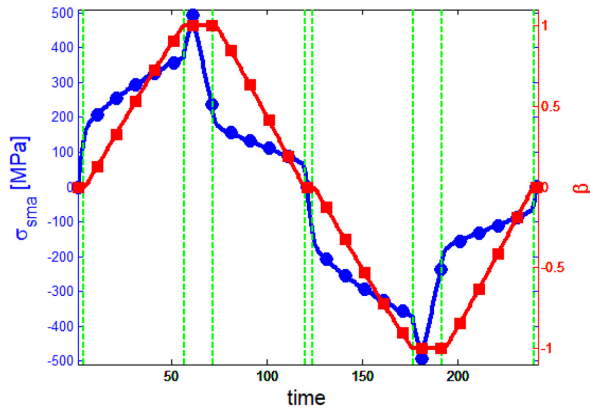


**Figure 4.** Stress (blue circles) and martensite (red squares) time histories for a prescribed uniform strain rate.

finishing temperatures for austenitic formation, respectively. For martensite, this reference temperatures are  $M_s$  and  $M_f$  (Savi et al., 2016). The tension-induced martensite is denoted by  $M^+$ , while  $M^-$  is the compression compression-induced martensite, and  $A$  means the austenitic phase. By observing the stress–strain curve, it should be noted that initially, the SMA is on austenitic phase ( $\beta = 0$ ). The tensile loading promotes an elastic response (green line) until the forward phase transformation is induced, represented by the red line, finishing the transformation at the blue line that is associated with an elastic response on the martensitic phase ( $\beta = 1$ ). During the unloading process, an elastic response is achieved (blue line) until the reverse transformation initiates and the austenite appears again (red line). An elastic response occurs again in austenitic phase (green line) until the loading process is finished. The same process takes place for compressive loads, but at the end of the forward transformation,  $\beta = -1$  (cyan), representing a different variant of martensite. Phase transformations are related to a hysteresis loop, being associated with a dissipation energy per volume. Figure 4 shows the stress and martensite time histories considering a prescribed uniform strain rate. The green dashed lines indicate the beginning and the end of phase transformation.

A complete pseudoelastic cycle is associated with a hysteresis loop that dissipates  $7285 \text{ kJ/m}^3$ . Incomplete phase transformations are related to internal sub-loops that tend to dissipate an amount of energy that is directly related to the volume fraction  $\beta$ . In this regard, an analysis of dissipated energy is now of concern. During the loading–unloading process, there are two distinct energies: elastic energy and dissipated energy due to pseudoelasticity. In order to analyze the energy due to this process, it is considered three different loading cases, associated with distinct cycles (Figure 5). Initially, the SMA is subjected to an elastic load, up to  $P_1$  and then completely unloaded. The second case

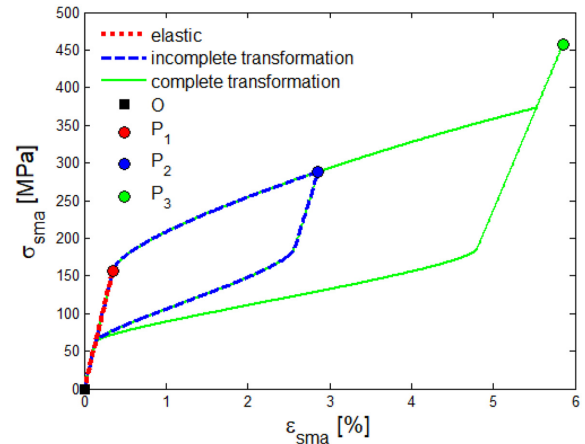


**Figure 5.** Stress–strain curve of the SMA representing the sub-loops.

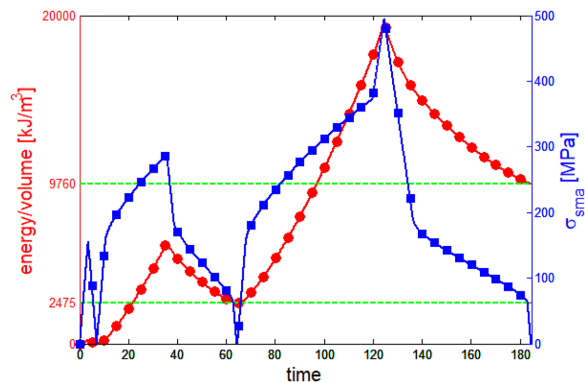


**Figure 6.** Total energy (red circles) and stress (blue squares) time histories for the prescribed uniform strain rate represented in Figure 5.

considers an incomplete phase transformation until point  $P_2$ , where  $\beta = 0.5$ . Finally, the third case is associated with a complete phase transformation until point  $P_3$  is reached ( $\beta = 1$ ). The energy per volume is calculated from the area under the stress–strain curve, which is performed by direct integration. The energy is added during the loading process (tension or compression) and subtracted during the unloading process. Figure 6 presents the total energy per volume together with stress time history. Figure 7 presents the total energy per volume together with the martensitic volume fraction evolution. The dashed horizontal green lines in Figures 6 and 7 represent the energy dissipated due to pseudoelasticity. Therefore, the energy dissipated during the first elastic cycle ( $P_1$ ) is zero since no phase transformation occurs, which means that the whole energy is released during unloading, without dissipation. However, when phase transformation occurs, there is a gap between the energy before and after the

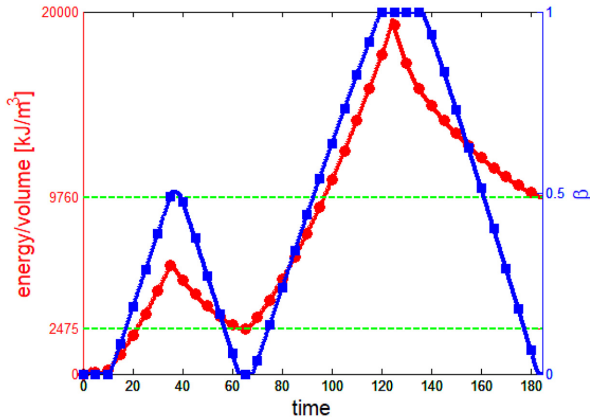


**Figure 7.** Total energy (red circles) and martensite (blue squares) time histories for the prescribed uniform strain rate represented in Figure 5.

cycle. Note that the second cycle ( $P_2$ ) has a dissipation of  $2475 \text{ kJ/m}^3$ . Finally, the last cycle that is associated with complete phase transformation ( $P_3$ ) has a dissipation estimated by the difference between the two levels of energy represented by the two dashed green lines ( $9760 - 2475 = 7285$ ), which is exactly the value calculated from the area of the hysteresis loop.

A simplified way to understand the relation between phase transformation and energy dissipation is assuming that both are proportional. For instance, if the complete hysteresis loop is able to dissipate  $7285 \text{ kJ/m}^3$ , during a complete phase transformation cycle, a sub-loop from associated with an incomplete phase transformation with  $\beta = 0.5$  dissipates  $3642.5 \text{ kJ/m}^3$ , half of the energy dissipated due to complete phase transformation. It should be highlighted that this is an approximation since the energy dissipated by a sub-loop with  $\beta = 0.5$  is  $2475 \text{ kJ/m}^3$ , as presented in Figures 6 and 7.

## 2.2. Matrix model

The modeling of matrix considers two different possibilities: an epoxy matrix, assumed to present a linear elastic behavior, and an aluminum, assumed to be elastoplastic. In general, both cases can be described by the elastoplastic constitutive equation, defined by considering a plastic strain,  $\varepsilon_m^p$

$$\sigma_m = E_m (\varepsilon_m - \varepsilon_m^p) \quad (12)$$

Note that elastic case is described assuming  $\varepsilon_m^p = 0$ . Plastic behavior considers that the yield surface has isotropic,  $\alpha$ , and kinematic,  $q$ , hardenings, being represented by the following flow laws (Simo and Hughes, 1997; Souza Neto et al., 2008)

$$\dot{\varepsilon}_m^p = \gamma h \text{sign}(\sigma_m - q) \quad (13)$$

**Table 2.** Matrices properties (Auricchio and Petrini, 2004; Freed and Aboudi, 2009).

Matrix	$E_m$ (GPa)	$S_y$ (MPa)	$h$ (GPa)	$K$ (GPa)
Epoxy	3.45	—	—	—
Aluminum	72.4	300	5	33.7

$$\dot{q} = \gamma h \text{sign}(\sigma_m - q) \quad (14)$$

$$\dot{\alpha} = \gamma \quad (15)$$

where  $h$  is the kinematic hardening modulus and  $\gamma$  is the plastic multiplier.

The yield surface is represented by the following condition

$$F_m(\sigma_m, q, \alpha) = |\sigma_m - q| - (S_y + K\alpha) \leq 0 \quad (16)$$

where  $K$  is the plastic modulus and  $S_y$  is the yield strength.

The Kuhn–Tucker and consistency conditions are expressed as follows

$$\gamma \geq 0, \quad F_m(\sigma_m, q, \alpha) \leq 0, \quad \gamma F_m(\sigma_m, q, \alpha) = 0 \quad (17)$$

$$\gamma \dot{F}_m(\sigma_m, q, \alpha) = 0 \quad \text{if} \quad F_m(\sigma_m, q, \alpha) = 0 \quad (18)$$

The material properties of matrices, epoxy and aluminum, are listed in Table 2.

## 2.3. Composite homogeneous model

The homogeneous description of the composite material is based on the fiber and matrix constitutive equations presented in the preceding sections. Therefore, the macroscopic model is represented by the following constitutive equation

$$\sigma = \sigma^0 + (E\varepsilon - E_0^* \varepsilon^0) - \varepsilon_R (E^* \beta - E_0^* \beta) \quad (19)$$

where  $E = V_{sma} E_{sma} + (1 - V_{sma}) E_m$ ,  $E^* = V_{sma} E_{sma}^*$ ,  $E_0^* = V_{sma} E_{sma}^{(0)}$ , and  $\sigma^0 = V_f \sigma_{sma}^0 - E_m \varepsilon_m^p$ .

In general, the following equation can be written as

$$\sigma = E\varepsilon - \varepsilon_R E^* \beta - f_0 \quad (20)$$

where  $f_0 = (\sigma^0 - E_0^* \varepsilon^0 + \varepsilon_R E_0^* \beta_{S_0})$  represents the initial state.

## 3. Structure dynamical model

The idea to investigate structures subjected to seismic loads is performed by considering an archetypal model that represents a one-story reinforced frame subjected to earthquake ground acceleration. Figure 8 presents this structural model highlighting the initial geometry composed by one floor over two columns of height  $H$  with two SMAC braces along the diagonals of length  $L$ .

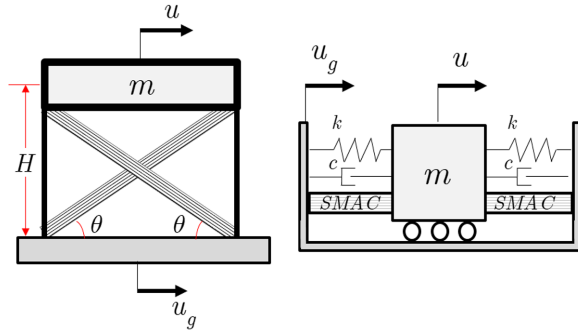


**Figure 8.** Dynamical model for the one-story frame under earthquake load.

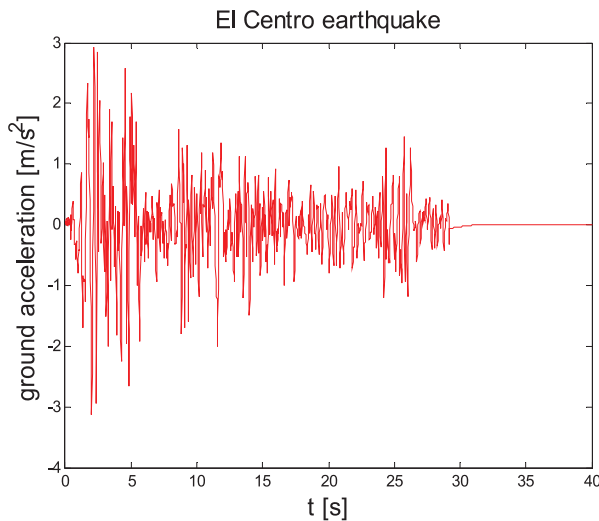


**Figure 9.** Ground acceleration related to El Centro earthquake with magnitude 7.1, which took place on 18 May 1940, Imperial Valley, USA (Vibrationdata, 2019).

The equivalent reduced order system is also presented. By assuming a relative displacement  $\bar{u} = u - u_g$ , where  $u_g$  is the ground displacement, the equation of motion is given by

$$\ddot{\bar{u}} + 2\xi\omega_n\dot{\bar{u}} + \omega_n^2\bar{u} + a\sigma \cos \theta = -\ddot{u}_g \quad (21)$$

where  $\omega_n = \sqrt{2k/m}$ ,  $\xi = c/m\omega_n$ ,  $a = 2A_b/m$ , and  $A_b$  is the braces' cross-sectional area. Besides,  $\beta = \beta(\sigma)$  and  $\sigma = \sigma(V_{sma}, \varepsilon)$  are defined from SMA constitutive equations presented in the previous section.

From kinematics analysis, the relation between the SMAC brace strain,  $\varepsilon$ , and the mass relative displacement,  $\bar{u}$ , is given by

$$\varepsilon = \frac{\Delta L}{L} = \frac{(u - u_g) \cos \theta}{(H/\sin \theta)} = \left(\frac{\bar{u}}{H}\right) \sin \theta \cos \theta \quad (22)$$

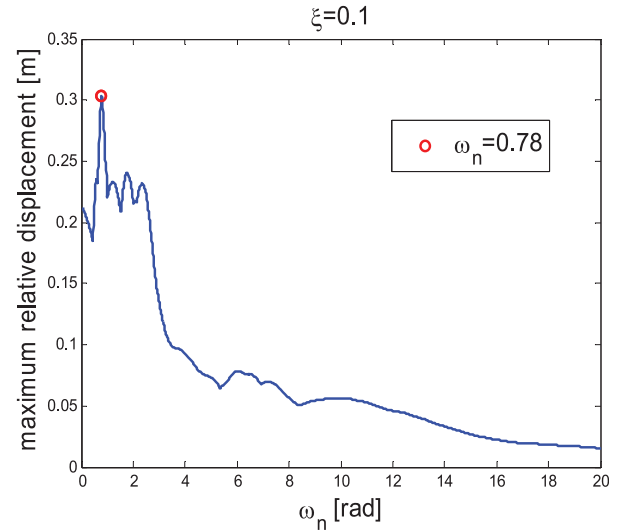


**Figure 10.** Maximum relative displacement of the elastic structure without reinforced braces.

Using the stress and strain of the SMA braces as defined by equation (19), equation (21) can be written as follows

$$\ddot{\bar{u}} + 2\xi\omega_n\dot{\bar{u}} + \left[\omega_n^2 + a\left(\frac{E}{H}\right) \sin \theta \cos^2 \theta\right] \bar{u} - a\varepsilon_R E^* \cos \theta \beta_S = -\ddot{u}_g - af_0 \cos \theta \quad (23)$$

The equation of motion is solved numerically using the fourth-order Runge–Kutta method following the procedure indicated by Savi (2015).

A case study is treated considering the ground acceleration data of the El Centro earthquake, 18 May 1940, Imperial Valley, USA, with magnitude 7.1 on the Richter scale, as presented in Figure 9 (Vibrationdata, 2019). Since different kinds of structures are subjected to the same seismic excitation, a parametric study is carried out to evaluate the critical case. Assuming that intrinsic dissipation of real structure is represented by a damping ratio  $\xi = 0.1$ , a structure without reinforced braces is considered to select the critical case. The idea is to define a natural frequency,  $\omega_n$ , associated with the highest amplitude subjected to the El Centro ground acceleration. Figure 10 indicates the maximum relative displacement, in absolute value, according to the natural frequency for  $\xi = 0.1$ . Based on this analysis, the critical case is defined for  $\omega_n = 0.78$  rad/s, which is used for all simulations.

Based on the theoretical development presented in the previous section, four parameters are required for the analysis:  $\omega_n$ ,  $\xi$ ,  $a$ , and  $V_{sma}$ . Natural frequency,  $\omega_n$  and dissipation,  $\xi$ , are assumed to be known, defining a critical situation. SMA volume fraction,  $V_{sma}$ , and parameter  $a$ , that establishes the relation between cross-

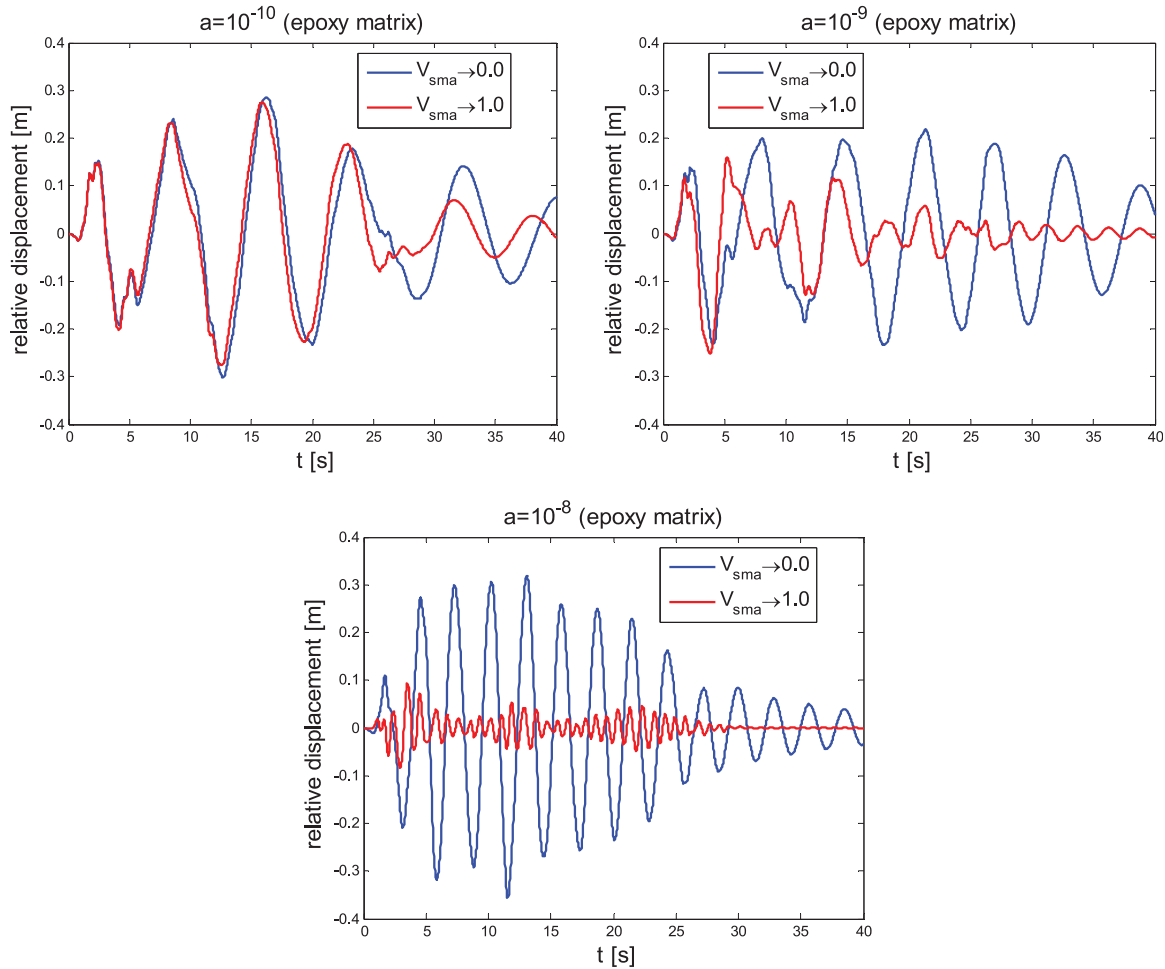


**Figure 11.** Time history of relative displacement for limit cases (pure matrix,  $V_{sma} \rightarrow 0.0$ , and pure SMA,  $V_{sma} \rightarrow 1.0$ ) for different values of parameter  $a$ :  $a = 10^{-10}$ ,  $a = 10^{-9}$ , and  $a = 10^{-8}$ .

sectional area and mass, are the design variables of the reinforced braces.

Initially, a SMAC with epoxy matrix is treated, considering two limit cases of SMA volume fraction:  $V_{sma} \rightarrow 0.0$  and  $V_{sma} \rightarrow 1.0$ . Note that  $V_{sma} \rightarrow 0.0$  means a brace without SMA while  $V_{sma} \rightarrow 1.0$  represents an SMA bar. It should be pointed out that as a matter of fact, there is a limitation of fiber volume fraction due to fiber packing arrangement, which means that these limit cases are usually not feasible (Barbero, 2018).

Different values of parameter  $a$  are analyzed for an epoxy matrix composite:  $a = 10^{-10}$ ,  $10^{-9}$ , and  $10^{-8}$ . Figure 11 presents relative displacements for all these parameters considering the limit cases: pure matrix,  $V_{sma} \rightarrow 0.0$ , and pure SMA,  $V_{sma} \rightarrow 1.0$ . Regarding the limit case  $V_{sma} \rightarrow 1.0$ , Figure 12 presents the martensitic evolution with respect to the time, Figure 13 indicates the stress–strain curves, and Figure 14 shows the total energy and the energy per volume, both represented by the elastic energy and the dissipated due to pseudoelasticity (phase transformation). Note that oscillatory part represents the elastic strain energy and the level change

represents the dissipated energy due to phase transformation. The difference between total energy and energy per volume in Figure 14 indicates the importance of the parameter  $a$ .

Since the braces are symmetrical, stress–strain, and martensitic phase, transformation energy time histories presented for one brace are the opposite of the other one. Energy time histories are similar. It is noticeable that the decrease of stiffness increases the amplitudes and increases the phase transformation and therefore, the dissipated energy. The increase of SMA volume fraction tends to increase the stiffness and therefore, reduce the dissipated energy per volume. Nevertheless, it increases the volume and, as a consequence, the total dissipated energy. Based on these arguments, it is clear that there are some mechanisms involved that need to be properly defined for design purposes. Based on this preliminary analysis, the focus is to consider parameter values of  $10^{-8} \leq a \leq 10^{-9}$ , assumed from now on.

The comparison between SMA composites with epoxy and aluminum matrices is now in focus. Figure 15 presents the variation of the maximum relative displacement according to  $a$  and  $V_{sma}$  for composites with



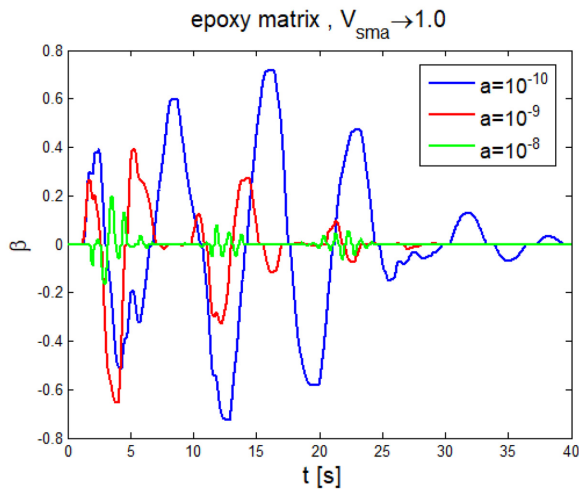


Figure 12. Martensite time history for  $V_{sma} \rightarrow 1.0$ .

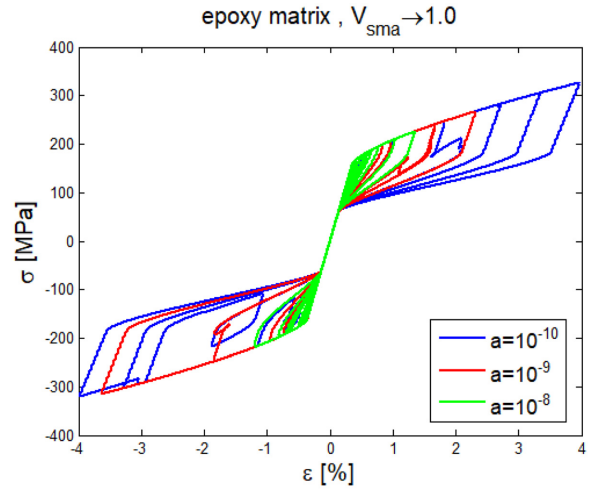


Figure 13. Stress-strain curves for  $V_{sma} \rightarrow 1.0$ .

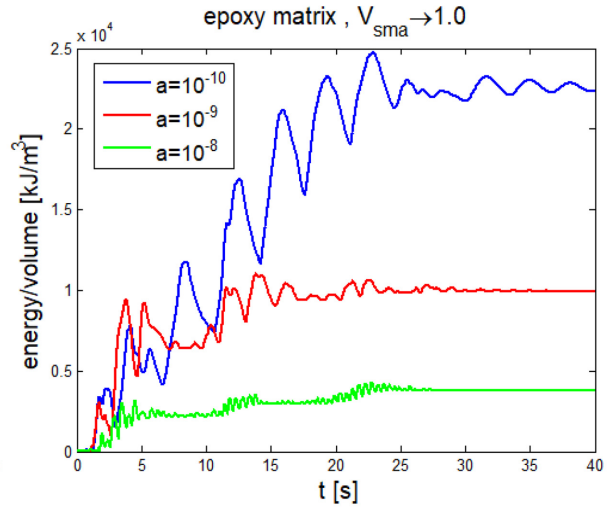
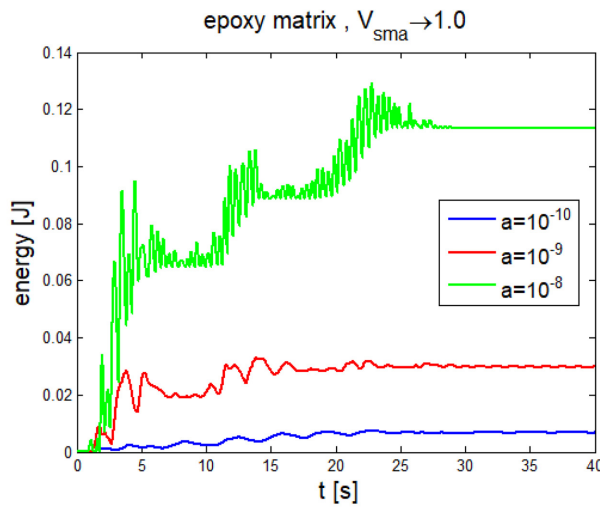


Figure 14. Total energy and energy per volume time history for each brace for  $V_{sma} \rightarrow 1.0$ .

epoxy (left) and aluminum (right) matrices. Results allow one to conclude the following:

1. Composite with epoxy matrix is more sensitive according to these parameters than the aluminum matrix composite.
2. The minimum amplitude, related to the optimum design condition, is similar for both cases, but with different combinations of  $a$  and  $V_{sma}$ .
3. Epoxy matrix results tend to have a better performance for higher volume fractions of SMA, while aluminum matrix does not have an evident trend depending on the value of  $a$ .

For a more comprehensive analysis, Figure 16 shows the maximum relative displacement according to  $V_{sma}$

for epoxy matrix and different values of  $a$ . Three main behaviors should be highlighted: the amplitude does not have a significant variation for  $1 \times 10^{-9} \leq a \leq 2 \times 10^{-9}$ ; a complex behavior appears for  $3 \times 10^{-9} \leq a \leq 6 \times 10^{-9}$ ; there is a plateau from a given value of  $V_{sma}$  for  $7 \times 10^{-9} \leq a \leq 10 \times 10^{-9}$ .

A proper design of the earthquake structure with SMA elements needs to observe the elastic and dissipated energies per volume, related to phase transformations, and the total amount of energy stored and dissipated, associated with the volume of the element. Two different structures are considered to illustrate these scenarios. The first one has a composite brace with small area, which means that its influence is not significant. Figure 17 presents results of this first kind of structure for  $a = 2 \times 10^{-9}$  and different values of

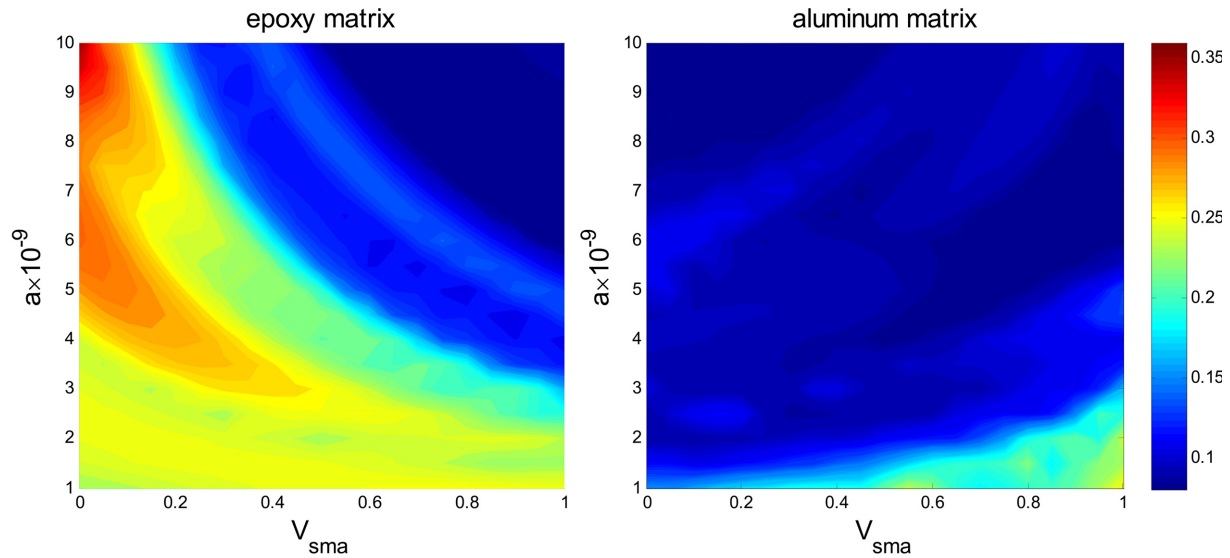


**Figure 15.** Influence of  $a$  and  $V_{sma}$  on the maximum relative displacement for composite braces with epoxy (left) and aluminum (right) matrices.

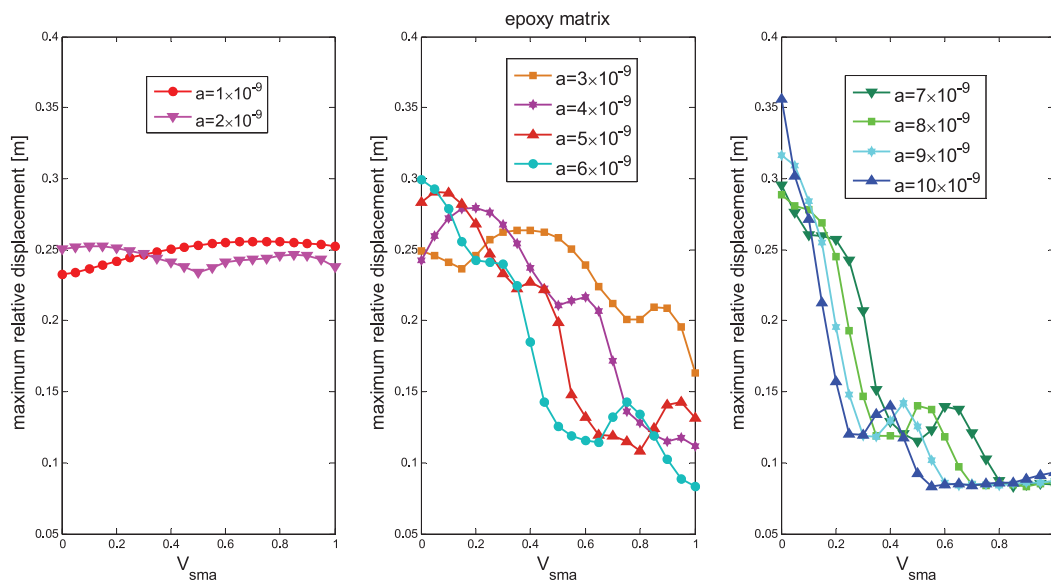


**Figure 16.** Maximum relative displacement according to  $V_{sma}$  for epoxy matrix.

SMA volume fraction,  $V_{sma} = 0.4, 0.6, 0.8$ . Despite the stress–strain curves are different, the area is still too small to decrease significantly the amplitude. The increase of parameter  $a$  changes this behavior. Figure 18 presents results for  $a = 5 \times 10^{-9}$  while Figure 19 shows results for  $a = 9 \times 10^{-9}$ . The stress level required for phase transformation initiation decreases if  $V_{sma}$  also decreases, but the size of the hysteresis loop, as well as internal sub-loops, is smaller for high values of  $V_{sma}$ . Hence, the composites with smaller values of  $V_{sma}$  tend to dissipate less energy. By comparing  $V_{sma} = 0.6$  and  $V_{sma} = 0.8$  for  $a = 9 \times 10^{-9}$ , the amplitudes are very close. Despite the complete hysteresis loop for

$V_{sma} = 0.8$  is larger than for  $V_{sma} = 0.6$ , the phase transformation is not complete for these cases studied. This complex behavior is due to these three concurrent mechanisms: stress level to initiate phase transformation, hysteresis loop, and the percent of phase transformation carried out, which influences the size of sub-loops.

The SMAC with aluminum matrix is now of concern. Figure 20 considers a parametric analysis showing maximum relative displacement with respect to SMA volume fraction and different values of parameter  $a$ . Note that for smaller braces' area, the dissipated energy due to matrix plastification is more significant than the

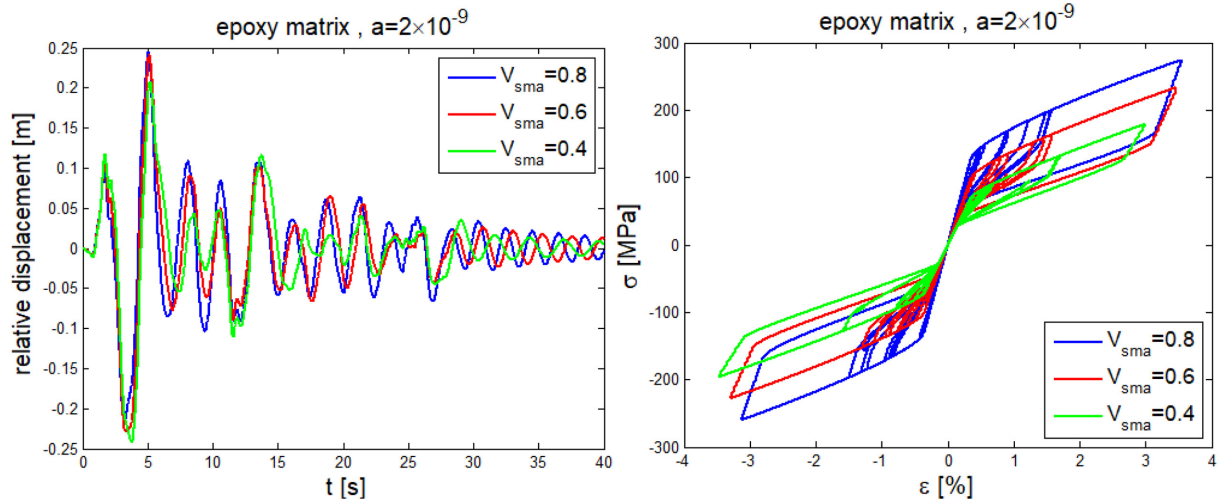


**Figure 17.** Relative displacement and stress–strain histories for braces of epoxy matrix with  $a = 2 \times 10^{-9}$  and  $V_{sma} = 0.4, 0.6, 0.8$ .

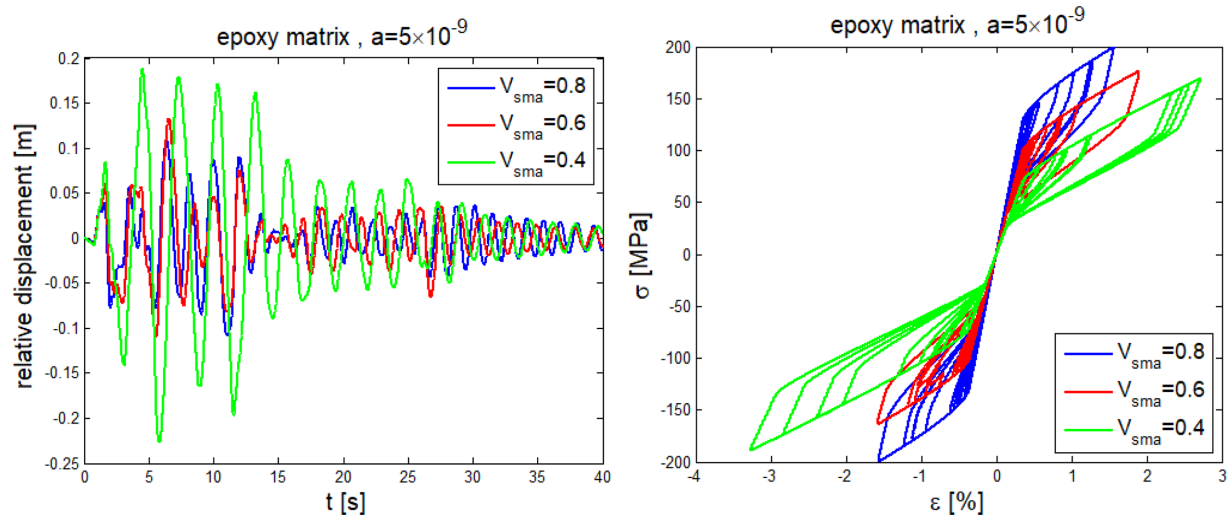


**Figure 18.** Relative displacement history for braces of epoxy matrix with  $a = 5 \times 10^{-9}$  and  $V_{sma} = 0.4, 0.6, 0.8$ .

dissipation due to SMA phase transformation. Plastic behavior should be highlighted in order to identify the main reason for the dramatic different responses. Figures 21 to 23 show the displacement and martensitic volume fraction time histories together with stress–strain curves. At the end of the process, a residual strain is observed on the relative displacement as well as a major influence of  $\beta$  induced by compression due to the asymmetric trend induced by matrix plasticity.

The residual displacement associated with the aluminum matrix yield is presented in Figure 24 for all the combinations of  $a$  and  $V_{sma}$  studied. Figure 25 shows a situation highlighting the residual displacement for  $a = 1 \times 10^{-9}$ . This result illustrates the complexity related to the design of composite materials: according to  $V_{sma}$ , keeping all the other parameters constant, the

residual displacement may be positive, negative, or null.

The advantage of the use of composite materials can be illustrated by evaluating the performance change with respect to the SMA volume fraction,  $V_{sma}$ . Figure 26 indicates that for  $a = 4 \times 10^{-9}$ , a composite with  $V_{sma} = 0.5$  dissipates more energy than a case with pure aluminum or SMA braces. A similar conclusion may be pointed out for  $a = 10 \times 10^{-9}$  according to Figure 27, but for this one the optimum condition is  $V_{sma} = 0.2$ . Note that this conclusion can be obtained by analyzing Figure 20, but these additional figures allow one to improve the compression with stress–strain curve along the whole period of time evaluated.

The developed analysis until now considers composite braces built by a homogeneous matrix (epoxy or

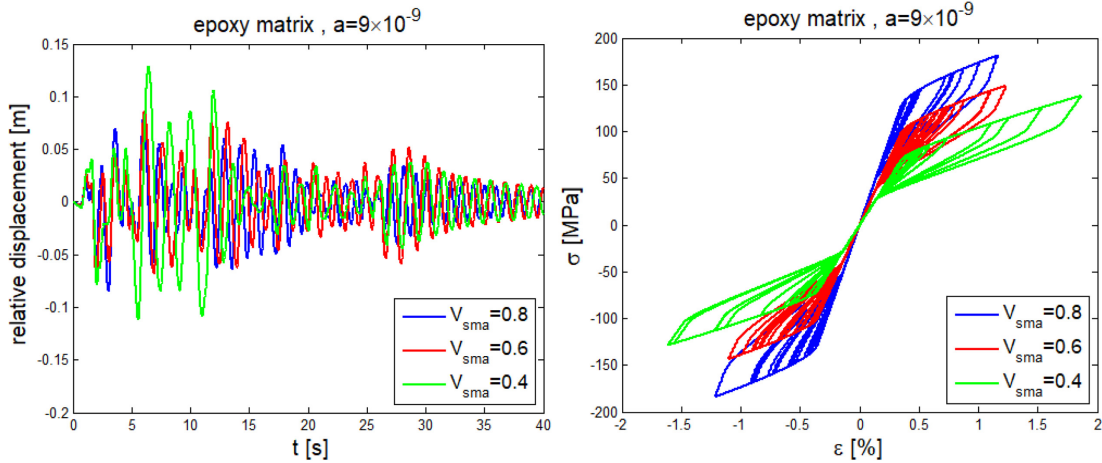


Figure 19. Relative displacement history for braces of epoxy matrix with  $a = 9 \times 10^{-9}$  and  $V_{sma} = 0.4, 0.6, 0.8$ .

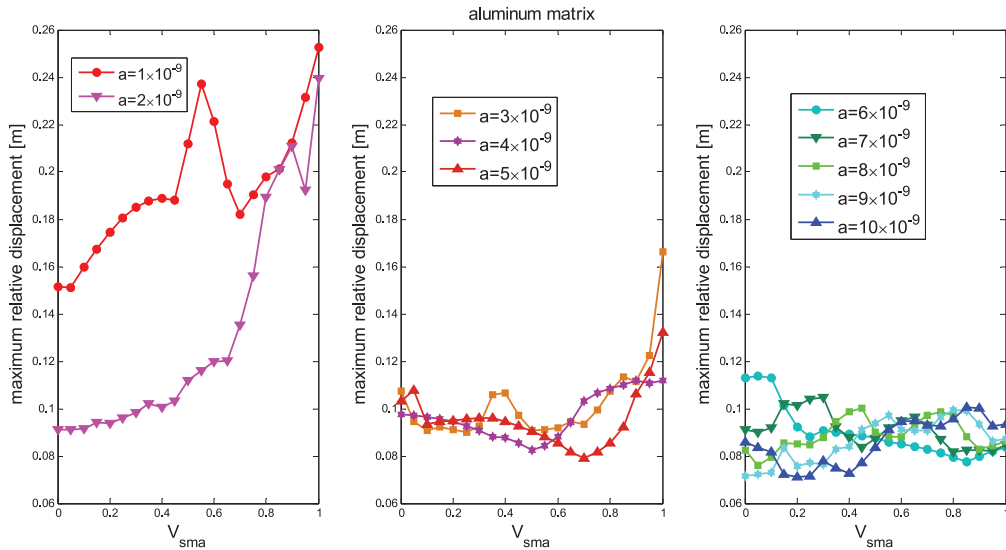


Figure 20. Maximum relative displacement according to  $V_{sma}$  for aluminum matrix.

aluminum) and SMA fibers. It should be pointed out that this implies a considerable difference between elastic moduli of both matrices (aluminum is around 20 times stiffer than the epoxy). Besides, it is assumed the yield capability of the aluminum, which is neglected for the epoxy. The matrix plasticity increases the energy dissipation, even though the residual strain is an unavoidable issue.

Based on this, it is important to evaluate the influence of the brace stiffness, without any additional effect, as plasticity. In order to deal with it, a hybrid composite is of concern considering the SMA with other elastic fibers (e.g. carbon or glass) in an epoxy matrix, increasing the elastic modulus. A simple modification must be done in order to describe this new hybrid composite:  $V_m + V_f + V_{sma} = 1$ , where  $V_f$  is the volume fraction of the additional elastic fiber.

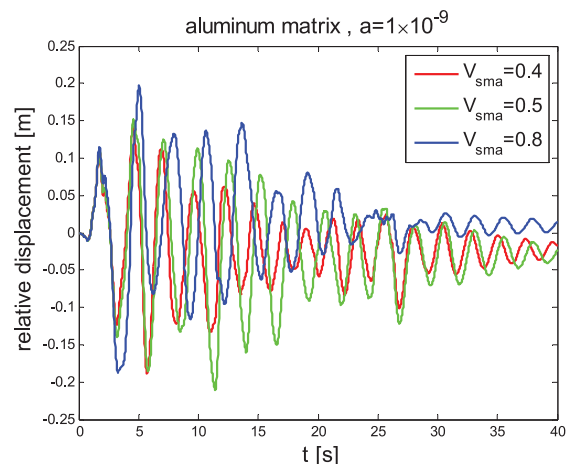
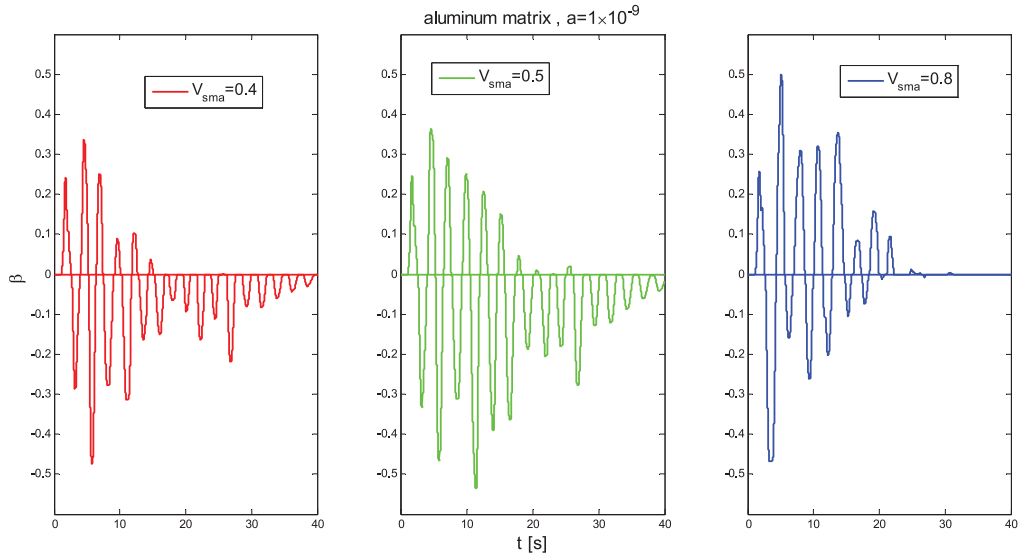
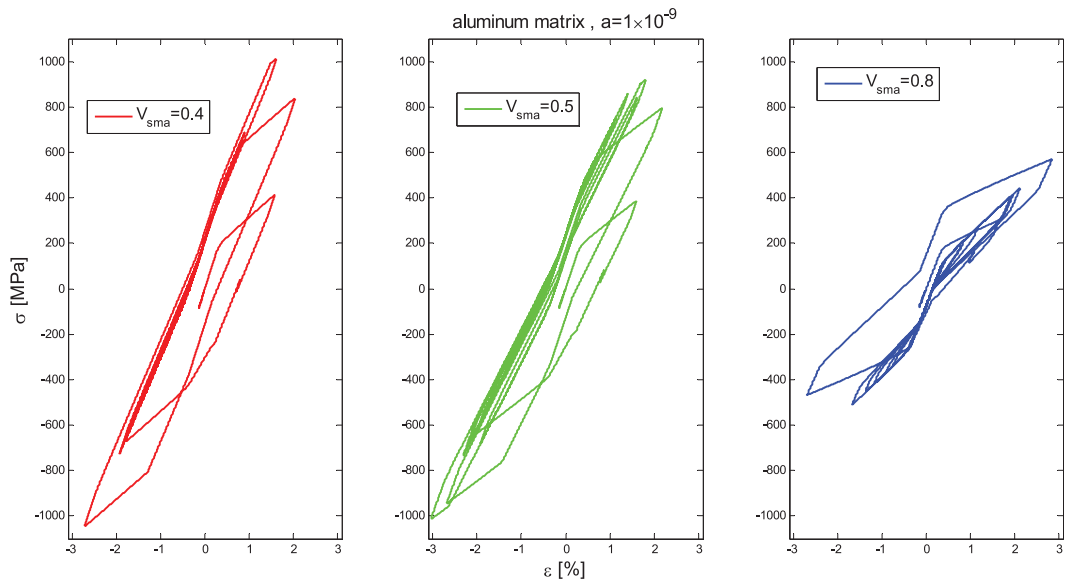


Figure 21. Relative displacement history for braces of aluminum matrix with  $a = 1 \times 10^{-9}$  and  $V_{sma} = 0.4, 0.5, 0.8$ .



**Figure 22.** Martensitic volume fraction time history for braces of aluminum matrix with  $a = 1 \times 10^{-9}$  and  $V_{sma} = 0.4, 0.5, 0.8$ .



**Figure 23.** Stress–strain curves for braces of aluminum matrix with  $a = 1 \times 10^{-9}$  and  $V_{sma} = 0.4, 0.5, 0.8$ .

Additionally, an equivalent elastic modulus needs to be considered:  $E_{eq} = E_m V_m + E_f V_f$ , where  $E_f$  is the fiber longitudinal elastic modulus (Vignoli et al., 2019).

Under these assumptions, the influence of the parameters  $a$  and  $V_{sma}$  on the maximum relative displacement for a reinforced structure with hybrid braces with  $E_{eq} = 72.4$  GPa is presented in Figure 28. Note that the equivalent elastic modulus is equal to the aluminum elastic modulus for a direct comparison with Figure 15. Figure 29 presents a comparative analysis for  $a = 5 \times 10^{-9}$  and  $a = 10 \times 10^{-9}$  considering the amplitude variation according to  $V_{sma}$  for epoxy and aluminum matrices and for the hybrid composites with  $E_{eq} = 72.4$  GPa. Both figures highlight the capability of

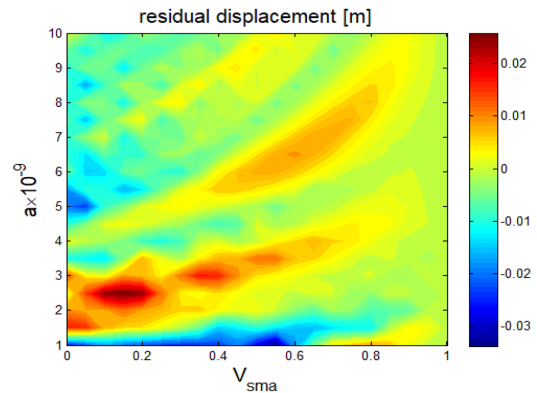


**Figure 24.** Residual displacement for reinforces with aluminum matrix.

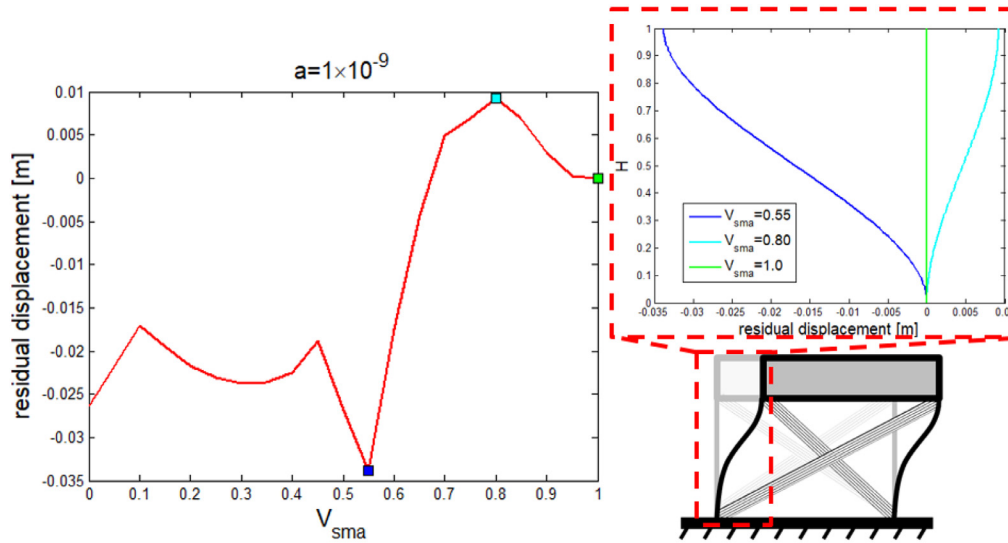


Figure 25. Residual displacement for a SMAC with aluminum matrix and  $a = 1 \times 10^{-9}$ .

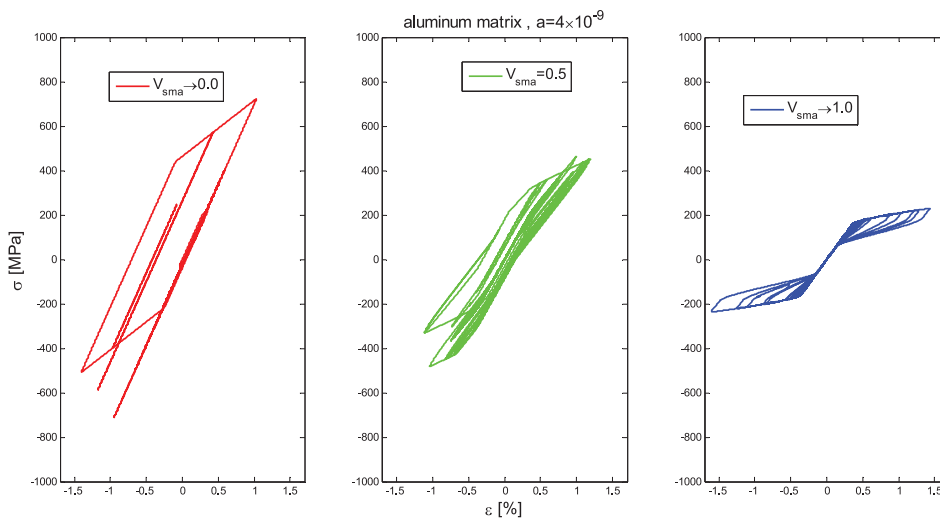


Figure 26. Stress-strain history for braces of aluminum matrix with  $a = 4 \times 10^{-9}$  and  $V_{sma} = 0.0, 0.5, 1.0$ .

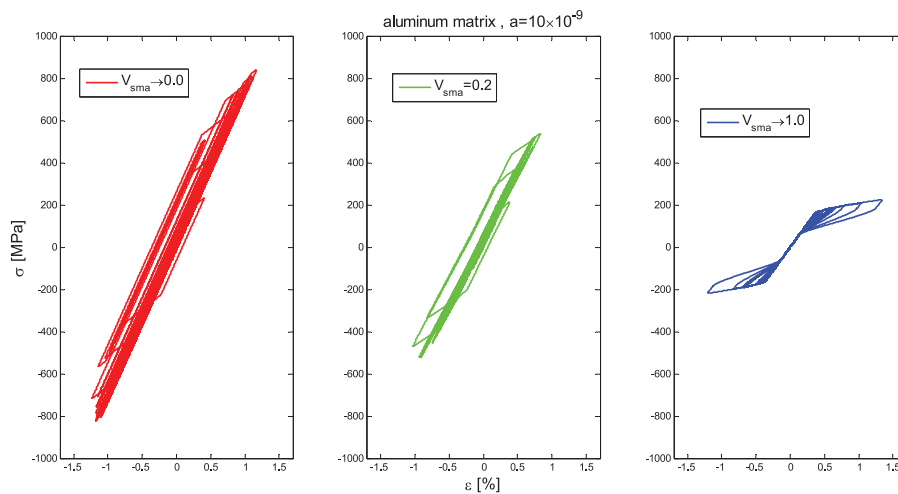
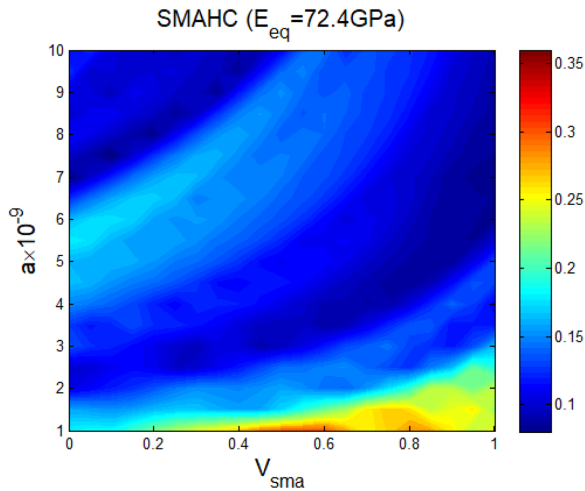


Figure 27. Stress-strain history for braces of aluminum matrix with  $a = 10 \times 10^{-9}$  and  $V_{sma} = 0.0, 0.2, 1.0$ .



**Figure 28.** Influence of  $a$  and  $V_{sma}$  on the maximum relative displacement for hybrid composite braces with  $E_{eq} = 72.4$  GPa.

SMA hybrid composites to either decrease the amplitude of the movement or eliminate the residual strain.

#### 4. Conclusion

Earthquake-resistant structures are investigated considering the dynamical behavior of one-frame structure reinforced with SMAC braces. The composite structure has a rich response with great influence of SMA volume fraction and matrix type. Numerical simulations show the design capability with SMAC to decrease vibration amplitude and increase dissipated energy. The importance of theoretical parametric studies is highlighted due to a large number of variables involved and the possibility to predict the optimal conditions for design

purposes. The influence of constituents' volume fractions, braces' area, and matrix type is discussed, including matrix nonlinearity induced by plasticity. This large variety of possibilities is prohibitive to be reached with experimental procedures. In general, the following conclusions should be pointed out. SMA is an interesting material to be associated with earthquake-resistant structures due to its high dissipation capacity due to hysteretic behavior. The use of SMA composite is probably the best strategy to exploit the dissipation capacity of SMAs. Different appropriate designs can be developed considering the SMA volume fraction becomes one design variable. In this regard, there is a competition among different phenomena in order to define the best configuration. Results indicate that the increase of the SMA volume fraction increases the dissipated energy per volume due to complete hysteresis loop associated with complete phase transformation. Nevertheless, the increase of the SMA volume fraction also alters the stiffness and the new configuration may be related to incomplete phase transformations, with different sub-loops. Another important point to be analyzed is the total energy, which is proportional to the parameter  $a$ . This also influences results altering the system stiffness. Based on that, the maximum value of SMA volume fraction does not coincide with the optimal condition for almost the whole range of  $a$  considered in this study. Considering different matrices, linear elastic matrix requires a higher volume fraction of SMA than elastoplastic matrix since plasticity also contributes to energy dissipation. Nevertheless, it is important to note that it is associated with undesirable residual strains. Alternatively, to increase the stiffness without residual strains due to aluminum matrix yield, the hybrid composites are discussed. Results indicate that join SMA and other elastic fibers, such as glass

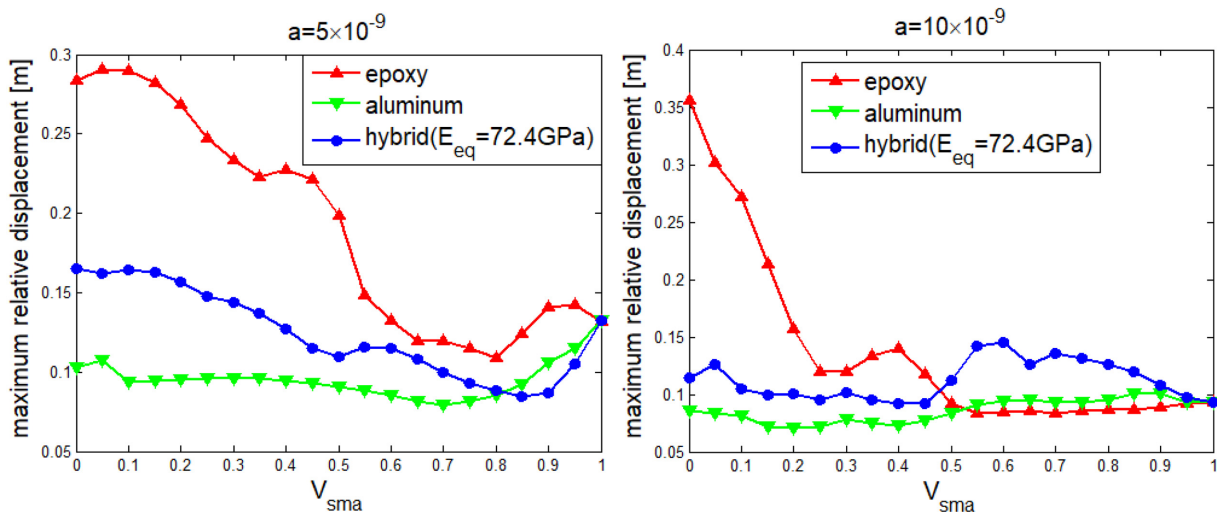


**Figure 29.** Comparison of the maximum relative displacement for composites with epoxy and aluminum matrix and hybrid composites.

and carbon, may increase the braces' stiffness and eliminate residual strain.

### Acknowledgements

The authors would like to acknowledge the Brazilian Research Agencies CNPq, CAPES, and FAPERJ, and The Air Force Office of Scientific Research (AFOSR).


### Declaration of conflicting interests

The author(s) declared no potential conflicts of interest with respect to the research, authorship, and/or publication of this article.

### Funding

The author(s) disclosed receipt of the following financial support for the research, authorship, and/or publication of this article: This study was supported by the Qatar National Research Fund through grant number NPRP 10-1204-160009.

### ORCID iD

Marcelo A Savi  <https://orcid.org/0000-0001-5454-5995>

### References

- Abou-Elfath H (2017) Evaluating the ductility characteristics of self-centering buckling-restrained shape memory alloy braces. *Smart Materials and Structures* 26: 055020.
- Alves MTS, Steffen Jr V, Santos MC, et al. (2018) Vibration control of a flexible rotor suspended by shape memory alloy wires. *Journal of Intelligent Material Systems and Structures* 29: 2309–2323.
- Asgarian B, Salari N and Saadati B (2016) Application of intelligent passive devices based on shape memory alloys in seismic control of structures. *Structures* 5: 161–169.
- Auricchio F and Petrini L (2004) A three-dimensional model describing stress-temperature induced solid phase transformations: thermomechanical coupling and hybrid composite applications. *International Journal for Numerical Methods in Engineering* 61: 716–737.
- Baratta A and Corbi O (2002) On the dynamic behaviour of elastic–plastic structures equipped with pseudoelastic SMA reinforcements. *Computational Materials Science* 22: 1–13.
- Barbero EJ (2018) *Introduction to Composite Materials Design*. 3rd ed. Boca Raton, FL: CRC Press.
- Billah AHMM and Alam MS (2012) Seismic performance of concrete columns reinforced with hybrid shape memory alloy (SMA) and fiber reinforced polymer (FRP) bars. *Construction and Building Materials* 28: 730–742.
- Boroschek RL, Farias G, Moroni O, et al. (2007) Effect of SMA braces in a steel frame building. *Journal of Earthquake Engineering* 11: 326–342.
- Brinson LC (1993) One-dimensional constitutive behavior of shape memory alloys: thermomechanical derivation with non-constant material functions and redefined martensite internal variable. *Journal of Intelligent Material Systems and Structures* 4: 229–242.
- Cardone D and Dolce M (2009) SMA-based tension control block for metallic tendons. *International Journal of Mechanical Sciences* 51: 159–165.
- Cisse C, Zaki W and Zineb TB (2016) A review of constitutive models and modeling techniques for shape memory alloys. *International Journal of Plasticity* 76: 244–284.
- Colalillo MA and Sheikh SA (2012) Seismic retrofit of shear-critical reinforced concrete beams using CFRP. *Construction and Building Materials* 32: 99–109.
- DesRoches R and Fenves GL (2000) Design of seismic cable hinge restrainers for bridges. *Journal of Structural Engineering* 126: 500–509.
- DesRoches R, Comerio M, Eberhard M, et al. (2011) Overview of the 2010 Haiti Earthquake. *Earthquake Spectra* 27: 1–21.
- Dolce M, Cardone D, Ponso FC, et al. (2005) Shaking table tests on reinforced concrete frames without and with passive control systems. *Earthquake Engineering and Structural Dynamics* 34: 1687–1717.
- Enemark S, Santos IF and Savi MA (2016) Modelling, characterisation and uncertainties of stabilized pseudoelastic shape memory alloy helical springs. *Journal of Intelligent Material Systems and Structures* 27: 2721–2743.
- Enemark S, Savi MA and Santos IF (2014) Nonlinear dynamics of a pseudoelastic shape memory alloy system: theory and experiment. *Smart Materials and Structures* 23: 085018.
- Eröz M and DesRoches R (2008) Bridge seismic response as a function of the Friction Pendulum System (FPS) modeling assumptions. *Engineering Structures* 30: 3204–3212.
- Fonseca LM, Rodrigues GV, Savi MA, et al. (2019) Non-linear dynamics of an origami wheel with shape memory alloy actuators. *Chaos, Solitons & Fractals* 122: 245–261.
- Freed Y and Aboudi J (2009) Micromechanical prediction of the two-way shape memory effect in shape memory alloy composites. *International Journal of Solids and Structures* 46: 1634–1647.
- Ghodke S and Jangid RS (2016) Equivalent linear elastic-viscous model of shape memory alloy for isolated structures. *Advances in Engineering Software* 99: 1–8.
- Johnson R, Padgett JE, Maragakis ME, et al. (2008) Large scale testing of nitinol shape memory alloy devices for retrofitting of bridges. *Smart Materials and Structures* 17: 035018.
- Khodaverdian A, Ghorbani-Tanha AK and Rahimian M (2012) An innovative base isolation system with Ni–Ti alloy and its application in seismic vibration control of Izadkhanst Bridge. *Journal of Intelligent Material Systems and Structures* 23: 897–908.
- Kim J and Jeong J (2016) Seismic retrofit of asymmetric structures using steel plate slit dampers. *Journal of Constructional Steel Research* 120: 232–244.
- Lagoudas DC (2008) *Shape Memory Alloys: Modeling and Engineering Applications*. Berlin: Springer.
- Lester BT, Baxevis T, Chemisky Y, et al. (2015) Review and perspectives: shape memory alloy composite systems. *Acta Mechanica* 226(12): 3907–3960.



- Li Y, Li J, Li W, et al. (2013) Development and characterization of a magnetorheological elastomer based adaptive seismic isolator. *Smart Materials and Structures* 22: 035005.
- Lu LY and Lin GL (2009) A theoretical study on piezoelectric smart isolation system for seismic protection of equipment in near-fault areas. *Journal of Intelligent Material Systems and Structures* 20: 217–232.
- Nehdi M, Alam MS and Youssef MA (2010) Development of corrosion-free concrete beam-column joint with adequate seismic energy dissipation. *Engineering Structures* 32: 2518–2528.
- Oliveira SA, Dornelas VM, Savi MA, et al. (2018) A phenomenological description of shape memory alloy transformation induced plasticity. *Meccanica* 53: 2503–2523.
- Oliveira SA, Savi MA and Zouain N (2016) A three-dimensional description of shape memory alloy thermomechanical behavior including plasticity. *Journal of the Brazilian Society of Mechanical Sciences and Engineering* 38: 1451–1472.
- Ozbulut OE, Hurlbauss S and DesRoches R (2011) Seismic response control using shape memory alloys: A review. *Journal of Intelligent Material Systems and Structures* 22: 1531–1549.
- Ozbulut OE and Hurlbauss S (2012) Application of an SMA-based hybrid control device to 20-story nonlinear benchmark building. *Earthquake Engineering and Structural Dynamics* 41: 1831–1843.
- Padgett J, DesRoches R, Nielson B, et al. (2008) Bridge damage and repair costs from hurricane Katrina. *Journal of Bridging Engineering* 13: 6–14.
- Paiva A and Savi MA (2006) An overview of constitutive models for shape memory alloys. *Mathematical Problems in Engineering* 2006: 56876.
- Qian H, Li H, Song G, et al. (2013) Recentering shape memory alloy passive damper for structural vibration control. *Mathematical Problems in Engineering* 2013: 963530.
- Rabiee R and Chae Y (2019) Adaptive base isolation system to achieve structural resiliency under both short- and long-period earthquake ground motions. *Journal of Intelligent Material Systems and Structures* 30: 16–31.
- Rodrigues GV, Fonseca LM, Savi MA, et al. (2017) Nonlinear dynamics of an adaptive origami-stent system. *International Journal of Mechanical Sciences* 133: 303–318.
- Saadat S, Noori M, Davoodi H, et al. (2001) Using NiTi SMA tendons for vibration control of coastal structures. *Smart Materials and Structures* 10: 695–704.
- Sahasrabudhe S and Nagarajaiah S (2005) Effectiveness of variable stiffness systems in base-isolated bridges subjected to near-fault earthquakes: an experimental and analytical study. *Journal of Intelligent Material Systems and Structures* 16: 743–756.
- Savi MA (2015) Nonlinear dynamics and chaos in shape memory alloy systems. *International Journal of Non-Linear Mechanics* 70: 2–19.
- Savi MA, Paiva A, Araujo CJ, et al. (2016) Shape memory alloys. In: Lopes V, Steffen V and Savi MA (eds) *Dynamics of Smart Systems and Structures*. 1st ed. New York: Springer, pp. 155–188.
- Shrestha KC, Saiidi MS and Cruz CA (2015) Advanced materials for control of post-earthquake damage in bridges. *Smart Materials and Structures* 24: 025035.
- Simo JC and Hughes TJR (1997) *Computational Inelasticity*. New York: Springer.
- Souza Neto EA, Peric D and Owen DRJ (2008) *Computational Methods for Plasticity: Theory and Applications*. Hoboken, NJ: John Wiley.
- Tsai SW and Melo JDD (2014) An invariant-based theory of composites. *Composites Science and Technology* 100: 237–243.
- U.S. Geological Survey (2019). Available at: <https://www.usgs.gov/>
- Vibrationdata (2019) Available at: <http://www.vibrationdata.com/elcentro.htm>
- Vignoli LL, Savi MA, Pacheco PMCL, et al. (2019) Comparative analysis of micromechanical models for the elastic composite laminae. *Composites Part B: Engineering* 174: 106961.
- Xu ZD (2007) Earthquake mitigation study on viscoelastic dampers for reinforced concrete structures. *Journal of Vibration and Control* 13: 29–43.
- Xu ZD (2009) Horizontal shaking table tests on structures using innovative earthquake mitigation devices. *Journal of Sound and Vibration* 325: 34–48.
- Xu ZD and Guo YQ (2006) Fuzzy control method for earthquake mitigation structures with magnetorheological dampers. *Journal of Intelligent Material Systems and Structures* 17: 871–881.
- Xu ZD, Gai PP, Zhao HY, et al. (2017) Experimental and theoretical study on a building structure controlled by multi-dimensional earthquake isolation and mitigation devices. *Nonlinear Dynamics* 89: 723–740.
- Yan S, Niu J, Mao P, et al. (2013) Experimental research on passive control of steel frame structure using SMA wires. *Mathematical Problems in Engineering* 2013: 416282.
- Yang CSW, DesRoches R and Leon RT (2010) Design and analysis of braced frames with shape memory alloy and energy-absorbing hybrid devices. *Engineering Structures* 32: 498–507.
- Yeghneem R, Meftah SA, Tounsi A, et al. (2009) Earthquake response of RC coupled shear walls strengthened with thin composite plates. *Journal of Vibration and Control* 15: 963–984.
- Zafar A and Andrawes B (2015) Seismic behavior of SMA-FRP reinforced concrete frames under sequential seismic hazard. *Engineering Structures* 98: 163–173.
- Zhang J, Wu Z, Zhang C, et al. (2019) Nonlinear dynamics of shape memory alloys actuated bistable beams. *Smart Materials and Structures* 28: 055009.
- Zhang J, Zhang C, Hao L, et al. (2017) Exploiting the instability of smart structure for reconfiguration. *Applied Physics Letters* 111: 064102.
- Zhang Y and Zhu S (2007) A shape memory alloy-based reusable hysteretic damper for seismic hazard mitigation. *Smart Materials and Structures* 16: 1603–1613.